An effective inversion strategy for fractal–multifractal encoding of a storm in Boston

Huai-Hsien Huang [a], Carlos E. Puente [a,*], Andrea Cortis [b], Juan L. Fernández Martínez [c]

[a] Land, Air & Water Resources, University of California, Davis, One Shields Ave., Davis, CA 95616, United States
[b] ION Geophysical Corporation, 2105 City West Blvd., Suite 900, Houston, TX 77042, United States
[c] Departamento de Matemáticas, Area de Matemática Aplicada, Universidad de Oviedo, Spain

SUMMARY

Hydrologic data sets such as precipitation records typically feature complex geometries that are difficult to represent as a whole using classical stochastic methods. In recent years, we have developed variants of a deterministic procedure, the fractal–multifractal (FM) method, whose patterns share not only key statistical properties of natural records but also the fine details and textures present on individual data sets. This work presents our latest efforts at encoding a celebrated rainfall data set from Boston and shows how a modified particle swarm optimization (PSO) procedure yields compelling solutions to the inverse problem for such a set. As our FM fits differ from the actual data set by less than 2% in maximum cumulative deviations and yield compression ratios ranging from 76:1 to 228:1, our models can be considered, for all practical purposes, faithful and parsimonious deterministic representations of the storm.

© 2013 Published by Elsevier B.V.

1. Introduction

Modeling of rainfall complexity has witnessed substantial progress in the past few decades, largely owing to the development of sophisticated mathematical techniques, such as those based on stochastic theories and fractal geometry. Although these ideas have resulted in a new language for the description and simulation of some of the data sets' intricacies, oftentimes these notions are still inadequate to study, on an individual basis, the incredible variety of natural rainfall patterns available to us.

Given that rainfall sets are typically erratic, noisy, intermittent, complex, or in short, "seemingly random," it has become natural to model them using stochastic (fractal) theories (e.g., Rodríguez-Iturbe, 1986; Lovejoy and Schertzer, 1990). This has inspired a variety of approaches that, while yielding realizations that preserve relevant statistical (physical) attributes of the records (e.g., moments, autocorrelation, power spectrum, multifractal spectrum, etc.), fail to capture specific details (e.g., positions of major peaks) and relevant textures (e.g., periods of no activity) present in measured data sets.

These limitations, intrinsic to any stochastic approach, led us to develop a fractal geometric methodology (e.g., Puente, 1996) aimed at capturing the complexity of rainfall patterns, and not just some key statistical features. By interpreting data sets as deterministic derived measures obtained transforming multifractals via fractal interpolating functions (e.g., Barnsley, 1988), our "fractal–multifractal" (FM) approach can indeed generate a vast class of patterns, over one or more dimensions, that encompasses all the distinctive characteristics of rainfall sets (e.g., Puente, 1996; Obregón et al., 2002a, 2002b) and other complicated geophysical patterns such as contaminant plumes in heterogeneous geological formations (e.g., Puente, 2004). This richness in the possibility of generating complex-looking deterministic sets with a relatively small number of parameters results, however, in a very intricate structure of the associated parameter space. Owing to this complexity, the solution of the inverse problem for a give data set, that is, searching for suitable FM parameters that produce a "match," remained, to date, an elusive task.

In this article, we report on our latest efforts to solve this very involved inverse problem. The proposed inversion strategy builds upon a recent generalization of the classical particle swarm optimization (PSO) search procedure (Fernández Martínez et al., 2010) that, combined with a statistical sampling of the initial conditions for the PSO, yields near-perfect parameter recovery for synthetic data sets and excellent fits of natural historic rainfall

* Corresponding author. Address: University of California, Davis, One Shields Ave., 127 Veihmeyer Hall, Davis, CA 95616, United States. Tel.: +1 530 752 0689; fax: +1 530 752 5262.
  E-mail address: cepuente@ucdavis.edu (C.E. Puente).

records, such as a detailed Boston storm used in earlier studies (Rodríguez-Iturbe et al., 1989; Puente and Obregón, 1996; Obregón et al., 2002b).

2. Materials and methods

In this section, we summarize the underlying mathematics of our FM geometric construction, including some of the extensions we have introduced, and outline the strategy for the solution of the inverse problem.

2.1. The original FM approach

In its simplest and original form, a FM pattern is obtained as the projection of the graph of a fractal interpolating function illuminated by a multifractal measure, as follows.

Firstly, the graph $G = \{(x, f(x)) | x \in [0, 1]\}$ of such a fractal function $f : x \to y$ passing by $N + 1$ ordered points along x, $\{(x_n, y_n) | x_0 < \ldots < x_N, n = 0, 1, \ldots, N\}$, is defined as the unique deterministic attractor of N simple affine maps: (Barnsley, 1988)

$$w_n \begin{pmatrix} x \\ y \end{pmatrix} = \begin{pmatrix} a_n & 0 \\ c_n & d_n \end{pmatrix} \begin{pmatrix} x \\ y \end{pmatrix} + \begin{pmatrix} e_n \\ f_n \end{pmatrix}, \quad n = 1, \ldots, N, \qquad (1)$$

where the vertical scaling parameters d_n satisfy $|d_n| < 1$, and the other parameters $a_n, c_n, e_n,$ and f_n are defined via the contracting initial conditions

$$w_n \begin{pmatrix} x_0 \\ y_0 \end{pmatrix} = \begin{pmatrix} x_{n-1} \\ y_{n-1} \end{pmatrix}, \qquad (2)$$

$$w_n \begin{pmatrix} x_N \\ y_N \end{pmatrix} = \begin{pmatrix} x_n \\ y_n \end{pmatrix}, \qquad (3)$$

which map the end values of the data in x into internal sub-intervals.

In a practical setting, the graph of a fractal function f, typically shaped as a convoluted wire and having a fractal dimension $1 \leqslant D < 2$, is obtained by a pointwise sampling of the attractor via iterations of the affine maps, a procedure also known as the chaos game (Barnsley, 1988). The idea is to start the process at a point already in G, e.g., a given (x_n, y_n), and progressively iterate the N maps w_n according to, for example, the outcomes of independent "coin" tosses.

Secondly, as the chaos game is performed for a sufficient amount of time, not only is the set G found, but also a unique invariant measure is induced over G, which reflects how the attractor is filled up. The existence of such a measure (akin to a histogram) allows computing unique—and hence, fully deterministic—projections over the coordinates x and y (denoted herein by dx and dy) that turn out to display irregular shapes as found in a variety of geophysical applications and beyond (see, e.g., Puente, 2004).

In order to clarify the notions, Fig. 1 shows an example of a fractal wire passing through the three points $\{(0, 0), (0.50, -0.35), (1, -0.20)\}$ as generated by 10^6 iterations of the two maps

$$w_1 \begin{pmatrix} x \\ y \end{pmatrix} = \begin{pmatrix} 0.50 & 0 \\ -0.51 & -0.80 \end{pmatrix} \begin{pmatrix} x \\ y \end{pmatrix} + \begin{pmatrix} 0 \\ 0 \end{pmatrix}, \qquad (4)$$

and

$$w_2 \begin{pmatrix} x \\ y \end{pmatrix} = \begin{pmatrix} 0.50 & 0 \\ 0.03 & -0.60 \end{pmatrix} \begin{pmatrix} x \\ y \end{pmatrix} + \begin{pmatrix} 0.50 \\ -0.35 \end{pmatrix} \qquad (5)$$

As may be readily verified, the two maps w_1 and w_2 satisfy the contractile Eqs. (2) and (3), operate in x over the intervals [0, 0.50] and [0.50, 1], respectively, and have vertical scaling parameters $d_1 = -0.8$ and $d_2 = -0.6$.
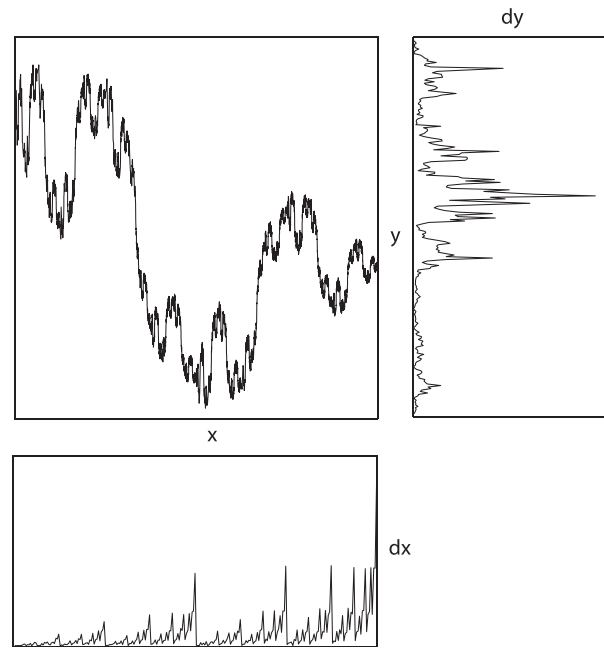

Fig. 1. The FM approach: from a multifractal dx to a projection dy via a fractal interpolating function, a wire from x to y.

In addition to the graph G, Fig. 1 also displays the projections (histograms) dx and dy, induced while carrying the previously mentioned chaos game according to a biased 30–70% proportion on w_1 and w_2.

As the x-coordinate in the maps is not affected by values of y (as implied by the zero entry in Eq. (1)), dx ends up being a simple deterministic (binomial) multifractal that, as it is related to a deterministic multiplicative cascade, exhibits noticeable repetition. In turn, dy happens to be the derived measure of dx via the fractal wire f and is computed, for any given value of y, by adding the corresponding "events" dx that satisfy $f(x) = y$. As can be seen, the geometrical FM construction generates a "random-looking" set dy that resembles a rainfall time series (e.g., Puente, 2004; Obregón et al., 2002b) and such is the basis for using such an approach, with suitable parameter values, to attempt to model hydrologic (geophysical) information.

Besides its clear geometric appeal, it happens that the FM approach may also be given a physical interpretation (Cortis et al., submitted for publication). For instance, as certain multifractals can be used to characterize energy distributions in turbulent atmospheric flows, the outputs dy may be interpreted as "reflections" (passive tracers) of turbulence or as non-trivial (fractal) integrations of rather spiky multifractals that reflect the phenomenology of random cascades. As the derived measures, for suitable sets of parameters, do share the spectrum of singularities of so-called "universal multifractals" (Tessier et al., 1993), they may also be thought of as specific realizations of random cascades, which have the advantage of being fully characterized, in their entirety, by a small set of parameters.

2.2. An extension with overlaps

The geometric procedure illustrated in Section 2.1 may be generalized so that the attractor G is no longer a function from x to y, but a "cloud" of points. This is accomplished by iterating N affine maps, as in Eq. (1), but replacing the contractive initial conditions by

$$w_n \begin{pmatrix} x_0 \\ y_0 \end{pmatrix} = \begin{pmatrix} x_{2n} \\ y_{2n} \end{pmatrix}, \tag{6}$$

and

$$w_n \begin{pmatrix} x_{2N-1} \\ y_{2N-1} \end{pmatrix} = \begin{pmatrix} x_{2n+1} \\ y_{2n+1} \end{pmatrix} \tag{7}$$

$n = 0, 1, \ldots, N - 1$, while satisfying a new ordering condition for values in x, namely: $x_0 \leqslant x_{2n} < x_{2n+1} \leqslant x_{2N-1}$.

As may be discerned, each one of the maps for this extension is associated with a set of endpoints that assign some new arbitrary subintervals in x, $[x_{2n}, x_{2n+1}]$, which are related with corresponding values in y, $[y_{2n}, y_{2n+1}]$. When these endpoints, from mapping to mapping, match both in x and y, this setting gives back the previously defined fractal interpolating function. However, when x-intervals overlap (e.g., when $x_{2n-1} > x_{2n}$), or when the endpoints in y do not match (when $y_{2n-1} \neq y_{2n}$), a more sophisticated attractor, not shaped as a single-valued function, emerges.

An example of these ideas is shown in Fig. 2, which exhibits a "leafy" attractor obtained by iterating the two maps

$$w_1 \begin{pmatrix} x \\ y \end{pmatrix} = \begin{pmatrix} 0.60 & 0 \\ 4.32 & 0.68 \end{pmatrix} \begin{pmatrix} x \\ y \end{pmatrix} + \begin{pmatrix} 0 \\ 0 \end{pmatrix} \tag{8}$$

and

$$w_2 \begin{pmatrix} x \\ y \end{pmatrix} = \begin{pmatrix} 0.70 & 0 \\ 1.52 & -0.52 \end{pmatrix} \begin{pmatrix} x \\ y \end{pmatrix} + \begin{pmatrix} 0.30 \\ 0 \end{pmatrix} \tag{9}$$

Here, w_1 and w_2 were used 36% and 64% of the time, and correspond to the endpoints $\{(0,0), (0.60, 5)\}$ and $\{(0.30, 0), (1, 1)\}$, respectively, which leads to an overlap in x as w_1 operates from 0 to 0.60 and w_2 does so from 0.30 to 1.

As shown in the figure, the unique projection over x is no longer a spiky multifractal but rather a smoother measure. However, its transformation via the rather structured fractal "leaf" yields yet another projection set over y that has also the typical features of a natural precipitation pattern and beyond.
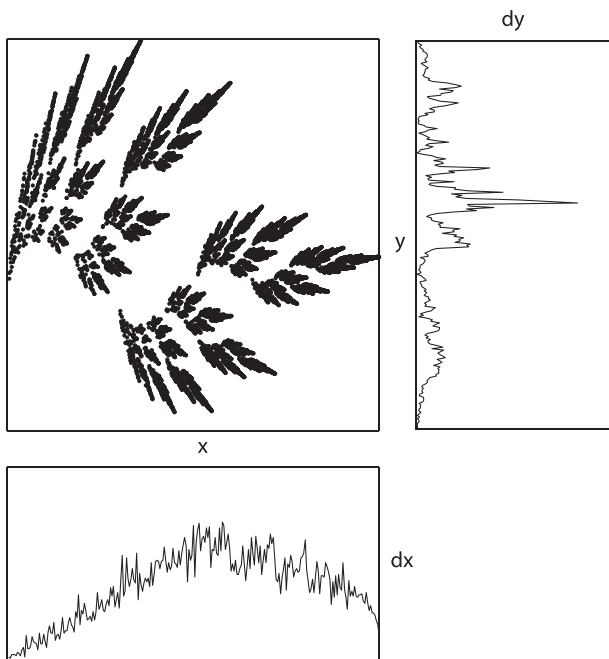
2.3. A nonlinear extension

Another way to extend the original FM procedure is to add a small nonlinear perturbation on each of the y-components of the affine mappings (e.g. a damped cosine function) (Cortis et al., 2009):

$$w_n \begin{pmatrix} x \\ y \end{pmatrix} = \begin{pmatrix} a_n & 0 \\ c_n & d_n \end{pmatrix} \begin{pmatrix} x \\ y + A_n \cos(\omega_n y) \end{pmatrix} + \begin{pmatrix} e_n \\ f_n \end{pmatrix}, \tag{10}$$

while keeping the same contractive initial conditions as in Eqs. (6) and (7).

An example of such an extension is seen in Fig. 3 for a setting of four regions of endpoints $\{(0, 0), (0.11, 1.36)\}$, $\{(0.56, -2.21), (0.75, -0.02)\}$, $\{(0.22, 2.02), (0.65, -2.59)\}$, and $\{(0.36, 4.49), (1, 1)\}$, corresponding to the maps,

$$w_1 \begin{pmatrix} x \\ y \end{pmatrix} = \begin{pmatrix} 0.11 & 0 \\ 1.00 & 0.34 \end{pmatrix} \begin{pmatrix} x \\ y + 0.37 * \cos(0.36y) \end{pmatrix} + \begin{pmatrix} 0 \\ -0.13 \end{pmatrix} \tag{11}$$

$$w_2 \begin{pmatrix} x \\ y \end{pmatrix} = \begin{pmatrix} 0.19 & 0 \\ 2.12 & 0.05 \end{pmatrix} \begin{pmatrix} x \\ y + 1 * \cos(0.76y) \end{pmatrix} + \begin{pmatrix} 0.56 \\ -2.26 \end{pmatrix} \tag{12}$$

$$w_3 \begin{pmatrix} x \\ y \end{pmatrix} = \begin{pmatrix} 0.43 & 0 \\ -4.33 & -0.24 \end{pmatrix} \begin{pmatrix} x \\ y + 0.44 * \cos(0.84y) \end{pmatrix} + \begin{pmatrix} 0.22 \\ 2.12 \end{pmatrix} \tag{13}$$

$$w_4 \begin{pmatrix} x \\ y \end{pmatrix} = \begin{pmatrix} 0.64 & 0 \\ -4.12 & 0.61 \end{pmatrix} \begin{pmatrix} x \\ y + 0.64 * \cos(0.37y) \end{pmatrix} + \begin{pmatrix} 0.36 \\ 4.10 \end{pmatrix}, \tag{14}$$

which, when iterated according to the proportions 9–18–20–53%, yield the attractor and related stable projections, over x and y, as depicted.

As may be seen, the new attractor G corresponding to the iterations of these (still simple) maps cannot be described either as a wire or a leaf. It also contains gaps over x that emanate from the propagation (via the four maps) of the unaccounted region in x

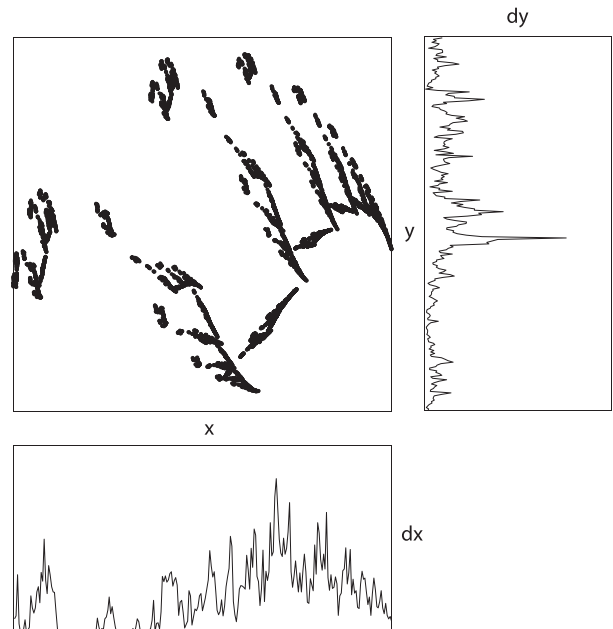**Fig. 2.** The FM approach with overlaps: from an input texture dx to a projection dy via a "leafy" attractor.

Fig. 3. The FM approach with nonlinear addition: from an input texture with holes dx to a projection dy via a "broken" attractor.

Table 1
Breakdown of errors (ℓ^2-norm of averaged cumulative function) over 100 runs for GPSO.

Set	# Maps	⩽1%	⩽2%	⩽5%	⩽10%	>10%
Boston	2	2	88	100	100	0
	3	41	97	100	100	0
	4	49	99	100	100	0
Synth	2	4	43	100	100	0
	3	2	95	100	100	0
	4	12	96	100	100	0

Table 2
Breakdown of errors (ℓ^2-norm of averaged cumulative function) over 100 runs for the classical PSO.

Set	# Maps	⩽1%	⩽2%	⩽5%	⩽10%	>10%
Boston	2	0	0	33	72	28
	3	0	0	66	97	3
	4	0	0	64	93	7
Synth	2	0	0	23	70	30
	3	0	0	0	52	48
	4	0	0	0	43	57

Table 3
Average improvement of the error over 100 runs.

Set	# Maps	Classical PSO (%)	GPSO (%)
Boston	2	20	52
	3	30	64
	4	38	71
Synth	2	21	53
	3	33	69
	4	35	75

from 0.11 to 0.22 as discerned from the endpoints above. Notice however how such an attractor still yields an interesting projection pattern over y (and also over x) that displays, once again, typical features of natural precipitation and other geophysical sets, hence defining a suitable extension for the description of complex data sets.

2.4. An extension from higher dimensions

The examples thus far have yielded attractors over two dimensions, but the geometric procedure can also be extended so that the attractor G is embedded in higher dimensional space.

Introducing a z-coordinate into the first generalization of the wire (that is, the overlapping extension) results in a map in the form of

$$w_n \begin{pmatrix} x \\ y \\ z \end{pmatrix} = \begin{pmatrix} a_n & 0 & 0 \\ d_n & r_n^{(1)} \cos\theta_1 & -r_n^{(2)} \sin\theta_2 \\ g_n & r_n^{(1)} \sin\theta_1 & r_n^{(2)} \cos\theta_2 \end{pmatrix} \begin{pmatrix} x \\ y \\ z \end{pmatrix} + \begin{pmatrix} l_n \\ m_n \\ n_n \end{pmatrix} \quad (15)$$

which, coupled with three-dimensional analogs of Eqs. (6) and (7), yields marginal projections over y and z that still resemble patterns of precipitation.

An increase in the dimensionality of the construction results in an increase in the number of parameters that specify the new affine mappings, as the previous vertical scaling parameters now become matrices (shown here in polar coordinates), but such does not alter the deterministic nature of the associated derived measures. Illustrations of such derived projections will be given in Section 3 when we will consider their application to the encoding of a measured rainfall dataset.

2.5. Solving the inverse problem

While the generation of FM patterns is computationally straightforward, the corresponding inverse problem, i.e., finding
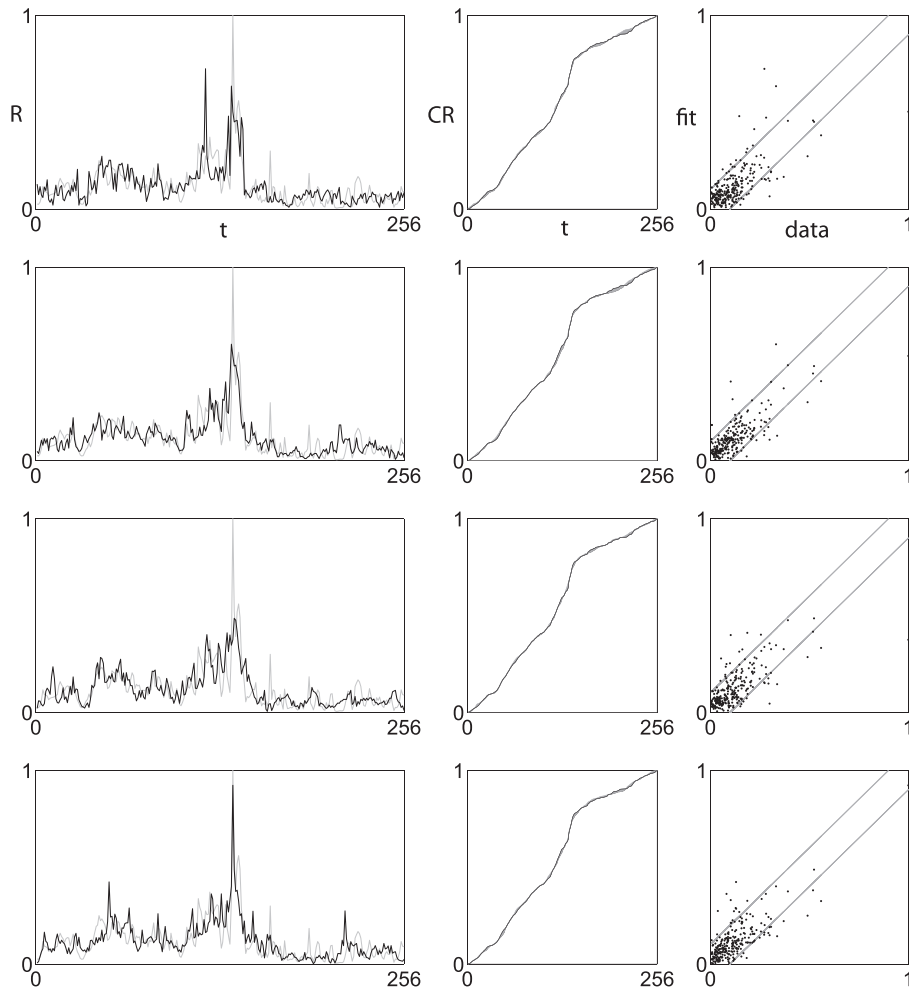
Table 4
Results of searching for a fit of the Boston storm made of 256 data points. Error 1, ℓ^2-norm of averaged cumulative deviation; Error 2, maximum cumulative deviation, and Error 3, percentage of data points that fall outside the ± 10% lines. Starred results denote entries used later to define Table 5.

Procedure	# Maps	# Parameters	Error 1 (%)	Error 2 (%)	Error 3 (%)
FM-Wire	3	9	0.73	2.14	14
	3	9	0.77	2.04	8
	4	13	0.58	2.55	11
	4*	13	0.68	1.75	12
FM-Leaf	3	13	0.51	2.18	10
	3	13	0.57	1.66	10
	4	17	0.47	1.35	13
	4*	17	0.43	1.54	7
FM-Nonlinear	2	11	0.59	1.51	12
	3*	19	0.52	1.35	9
	4	25	0.51	1.35	12
	4	25	0.55	1.40	11
FM-Marginal	2	16	0.64	1.54	12
	2	16	0.66	1.82	11
	3*	27	0.50	1.40	9
	3	27	0.56	1.65	17

Fig. 4. Boston renderings using the original FM approach. Left column: the fit, in black, imposed on the original data, in gray. Middle column: the cumulative functions of the data and the fit, with errors colored as area between the curves. Right column: scattergram of the data (horizontal) vs. the fit (vertical). Diagonal lines indicate ±10% lines. From top to bottom, the representations were constructed using three, three, four, and four maps. Readers interested in reconstructing the plots may navigate to the website, where all parameters may be found: http://puente.lawr.ucdavis.edu/omake/jhydro2012.html.

the FM mappings and the associated iterating frequencies that closely approximate a given dataset, presents distinct challenges that are associated with: (i) the high dimensionality of the search space, (ii) the ambiguity in the choice of the objective function to be minimized, (iii) the complexity of the corresponding objective function landscape, and (iv) the choice of the minimization algorithm, its parameters and search strategy.

Over the years, we have used a number of alternative optimization techniques coupled with various objective functions to attempt a solution of the FM inverse problem, including multidimensional simplex approaches, genetic algorithms, differential evolution, and various implementations of the particle swarm optimization (e.g., Obregón et al., 2002a; Puente and Sivakumar, 2007). At the same time, we have tested various objective functions, among others, fitting ℓ^2- and ℓ^1-norms (that is, the square root of sums of squares and the sum of absolute values, respectively) of one or more of the attributes of the records, such as the records themselves, their moments, autocorrelations and power spectra, multifractal spectra, cumulative function, Fourier and Stieltjes transforms, and the record's envelope. We also considered the Wasserstein metric, also known as the earth mover's distance (Hitchcock, 1941), to test whether non-local effects in the objective function may lead to improved solutions.

During our efforts we have learned that the fitness landscapes, on the space of parameters, are indeed fairly complex, even when there are only a handful of parameters. It is therefore easy to get trapped in local minima, irrespective of the optimization technique and the objective function employed. This observation holds true even when using synthetic sets as reality and while starting a search from initial solutions that are relatively close to the original generating parameters. Also, as may be expected, the initial values used on a given search happen to greatly influence the quality of the final results.

Building on our extensive numerical experience, we recently arrived to the definition of an inversion strategy that is proposed in this paper, which consists in considering a large set of randomly selected initial conditions to drive a generalized particle swarm optimization (GPSO) technique.

PSO algorithms are a class of heuristic optimization algorithms that are inspired by the collective social behavior of animals (Kennedy and Eberhart, 1995), and have been extensively used to complex optimization processes. A perceived limitation of the PSO method is its internal parameters calibration, which has until recently considered a matter of heuristic case-by case experimentation. In order to overcome this difficulty in the application of the PSO algorithm, Fernández Martínez et al. (2010) proposed to interpret the workings of the PSO process as a discretization of a stochastic damped mass-spring system. To test the proposed strategy, we chose to work with the centered-regressive discretization of the GPSO algorithm of Fernández Martínez et al. (2010). The GPSO algorithm can summarize by the following simple steps:
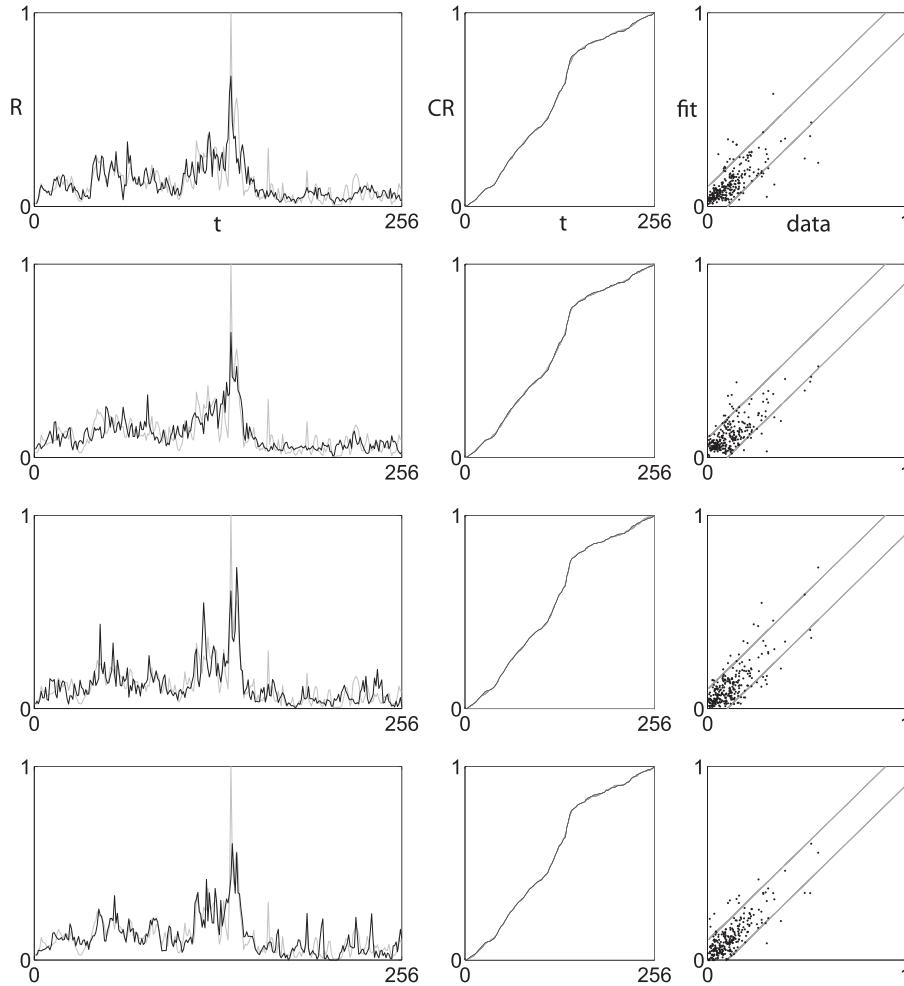
Fig. 5. Boston renderings using the overlapping extension. The column setup is as in Fig. 4. From top to bottom, the representations were constructed using three, three, four, and four maps.

(1) Define an m -dimensional space M of admissible model parameters: each of the parameters is bounded by lower and upper limits. A model in this parameter space is called a particle. m -dimensional vectors for position P and a velocity V in the search space characterize each particle. The notations P_j^k and V_j^k represent, respectively, position and velocity of particle j at time k.

(2) Define an n-dimensional particle swarm of potential models with positions $P_j^0, 1 \leqslant j \leqslant n$, randomly distributed in the space M of admissible parameters, and assign an initial zero velocity V_j^0 to each of the n particles. Calculate the misfit $E(P_j^0)$ to the data for each of the swarm particles, and calculate local best for each particle $L_j^k = \min_{P_j^i} E(P_j^i)$ for $1 \leqslant j \leqslant n$ and $0 \leqslant i \leqslant k$, and global best $G^k = \min_{L_j^k} E(L_j^k)$.

(3) Modify the position and velocity of each particle in the swarm according to a centered-regressive time discretization, $V_j^{k+dt} = \omega dt V_j^k + \phi_1 dt(G^k - P_j^k) + \phi_2 dt(L_j^k - P_j^k)$, and $P_j^{k+1} = V_j^{k+1} + P_j^k$, where $\phi_1 = r_1 a_G, \phi_2 = r_2 a_L$, $r_1, r_2 \in U(0,1)$ are uniformly distributed random variables, a_G are the global and local accelerations, and ω represents the inertia of the system, and dt is the time step.

A detailed treatment of the stability regions for this algorithm (and other related discretizations) can be found in (2010). In this work, we apply the "cloud" version of the GPSO algorithm, where all members of the swarm, in addition to the "leader," as originally proposed, have dynamic capabilities.

In this work, the swarm population consists of 300 particles, where each particle represents the set of generating parameters for a given FM projection (normalized in the range [0, 1]). Each particle of the PSO swarm is assigned its own inertia and global and local accelerations, chosen close to the limit of second-order stability of each PSO member to obtain a working compromise between the need to converge towards a minimum and the need to explore new portions of the search space. The swarm is then allowed to evolve for a total of 40 iterations.

Reported next are the results obtained by minimizing the ℓ^2-norm of averaged cumulative deviations,

$$\text{err} = \sqrt{\frac{1}{N_0}\sum_{n=1}^{N_0}(c_n - \hat{c}_n)^2} \tag{16}$$

where N_0 is the number of data points (256 in this case) and c_n and $\hat{c}_n$ are the nth accumulated values of the original records and the generated fit, respectively. Such an objective function was determined to provide visually reasonable and accurate sets while being
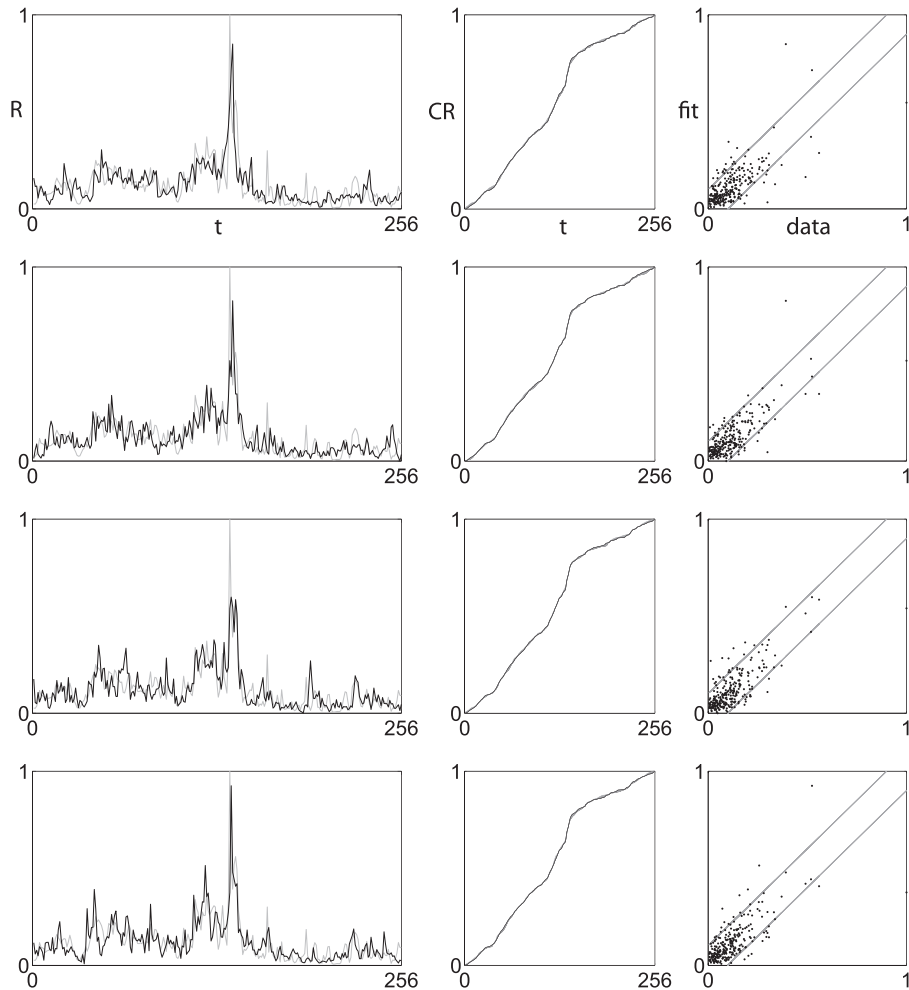
Fig. 6. Boston renderings using the nonlinear extension. The column setup is as in Fig. 4. From top to bottom, the representations were constructed using two, three, four, and four maps.

computationally efficient. In order to ensure that solutions shared geometrically similar features with the target set, we also imposed penalties on the objective function, such as demanding that the maximum cumulative deviations (pointwise) would not exceed anywhere a value of 10%.

2.6. Numerical tests of the inversion strategy

In order to assess the feasibility and efficacy of our inversion strategy, we tested our original FM procedure (using two, three, and four maps) on a number of synthetically generated and measured "real" data sets. What follows is a summary of these numerical experiments for two sets made of 256 data points: (a) one representative synthetic data set, labeled as "Synth," and obtained via the FM approach using two maps, and (b) the previously mentioned storm in Boston, labeled as "Boston," found aggregating from the original records so that the observations happen every 2 min.

Table 1 includes the ℓ^2-norm of averaged cumulative deviations (Eq. (16)) for the generalized particle swarm optimization (GPSO) runs considering 100 uniformly selected random initial conditions for the parameters. As can be seen in the table, all 100 runs yield errors consistently smaller than 5%, and the vast majority of them are smaller than 2% for the synthetic series (three and four maps) and for the Boston storm (two, three, and four maps). Curiously,

only four of the runs using two maps for the synthetic set (i.e., the case used in the definition of such a set) provide misfits smaller than 1% error, compared to the two and twelve runs for three and four maps, respectively. Furthermore, and as it can be seen, there were more successful runs at the 1% level for the Boston storm (especially for three and four maps) than for the synthetic set, an indication of the complexity of the landscape being searched.

Close examination of the results of the synthetic case reveals that the four best results listed on the table are indeed extremely close to the original parameters, virtually recovering the set perfectly. For the two and twelve best results in the three- and four-map runs (i.e., less than 1%), on the other hand, the parameters do exhibit more variation but they closely reproduce the synthetic set, despite belonging to rather distinct regions in parameter space, hence suggesting that there may not be a unique solution for a given set. These results for the synthetic set represent a significant step forward with respect to our past attempts at recovering the generating parameters of such sets or even at getting sufficiently close approximations of the patterns themselves. The plot comparisons between the used synthetic data set and its best fits are not reported here as the corresponding graphs are indeed virtually indistinguishable.

For the sake of comparison, Table 2 contains the same tests discussed in Table 1, but for the classical particle swarm optimization (PSO) algorithm, which exhibit a clear degraded performance. The
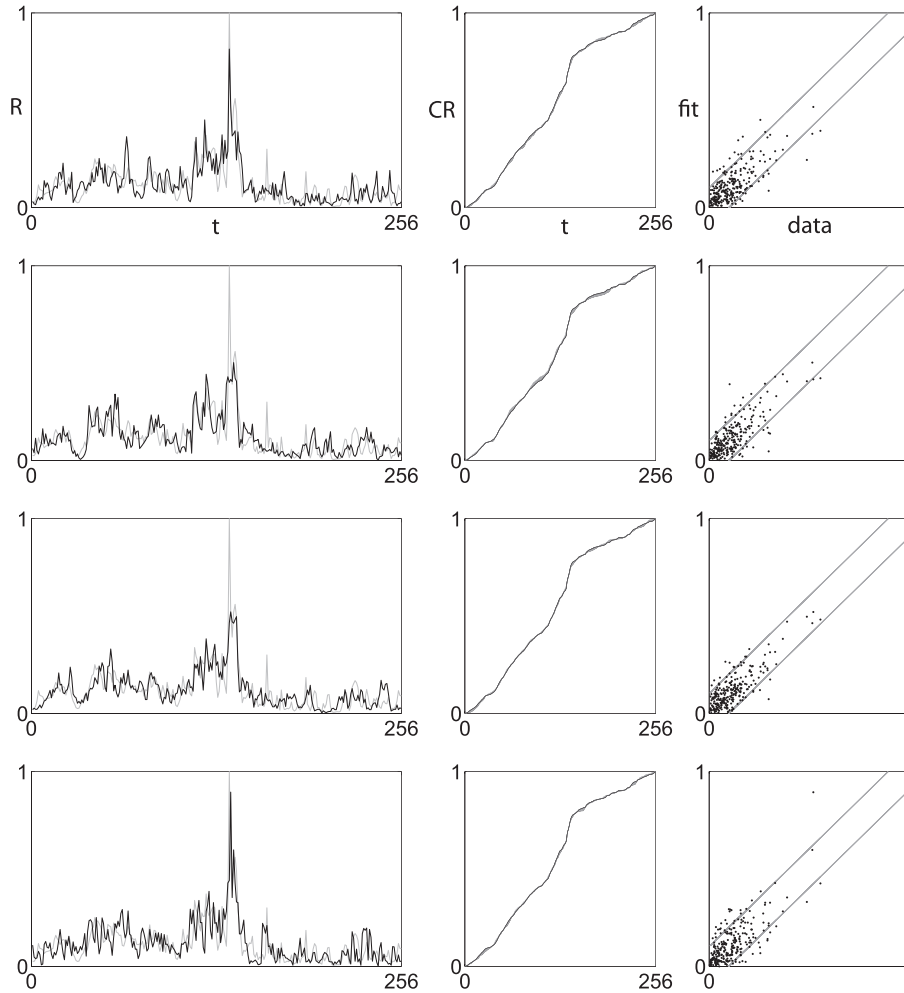
Fig. 7. Boston renderings using the higher-dimensional extension. The column setup is as in Fig. 4. From top to bottom, the representations were constructed using two, two, three, and three maps.

dramatic change in the quality of the fits can therefore only be attributed to the choice of the GPSO algorithm and not to the introduction of the ensemble of random initial conditions common to both approaches. Not only does the classical PSO algorithm fail to produce any solutions with errors less than 2% for the two sets in question, but it often leads to many cases with errors greater than 10%, regardless of the number of maps used, and even more so for the synthetic set.

As a note on computational times, on a modern quad-core (four CPUs, each clocking in at ∼3.4 GHz) desktop computer, a single 40-iteration run of the GPSO on the original "wire" procedure takes 30–36 s to complete, compared to the 6–9 min of the classical PSO. However, the latter is in reality considerably slower as there is much less improvement within the iterations when following just the leader of a swarm, as illustrated in Table 3.

3. Fitting the Boston storm with FM models

In this section, we apply the inversion strategy presented in Section 2.6 to find the parameters that best encode the Boston storm, not only for the original FM approach (FM-Wire) but also for the three FM extensions described in Sections 2.2-2.4, named, in order, FM-Leaf, FM-Nonlinear, and FM-Marginal.

Before showing specific results based on the alternative procedures, Table 4 lists general pertinent information for four renderings corresponding to each of the four FM models. Included in the table are the number of (affine) maps used in a given fitting and the corresponding number of parameters that holistically describe an approximation of the Boston storm, followed by relevant statistical information: Error 1 is the same as in Eq. (16), that is, the ℓ^2-norm of the averaged cumulative deviations, Error 2 represents the maximum cumulative deviation (not explicitly optimized in the procedure, though included as a 10% penalty as detailed in Section 2.5), and Error 3 is the percentage of points that lie outside the ±10% band of a scatter plot of real vs. fitted values.

As may be readily seen, a host of excellent fits for the Boston storm were obtained by the FM approaches as attested by the rather small errors in the reported attributes, and for representations that require from 9 to 27 parameters. While the ℓ^2-norm of averaged cumulative deviations are consistently lower than 0.80%, it is also noteworthy to observe that the maximum cumulative deviation seldom exceeds a mere 2% and that the percent of fitted values outside the scatter plot's ±10% bands is typically below 15%. It is also important to note, to be seen graphically later, that the deviations between the FM model and the data carry little information regarding a systematic bias as they are randomly distributed with zero mean. As shall be shown next for all FM
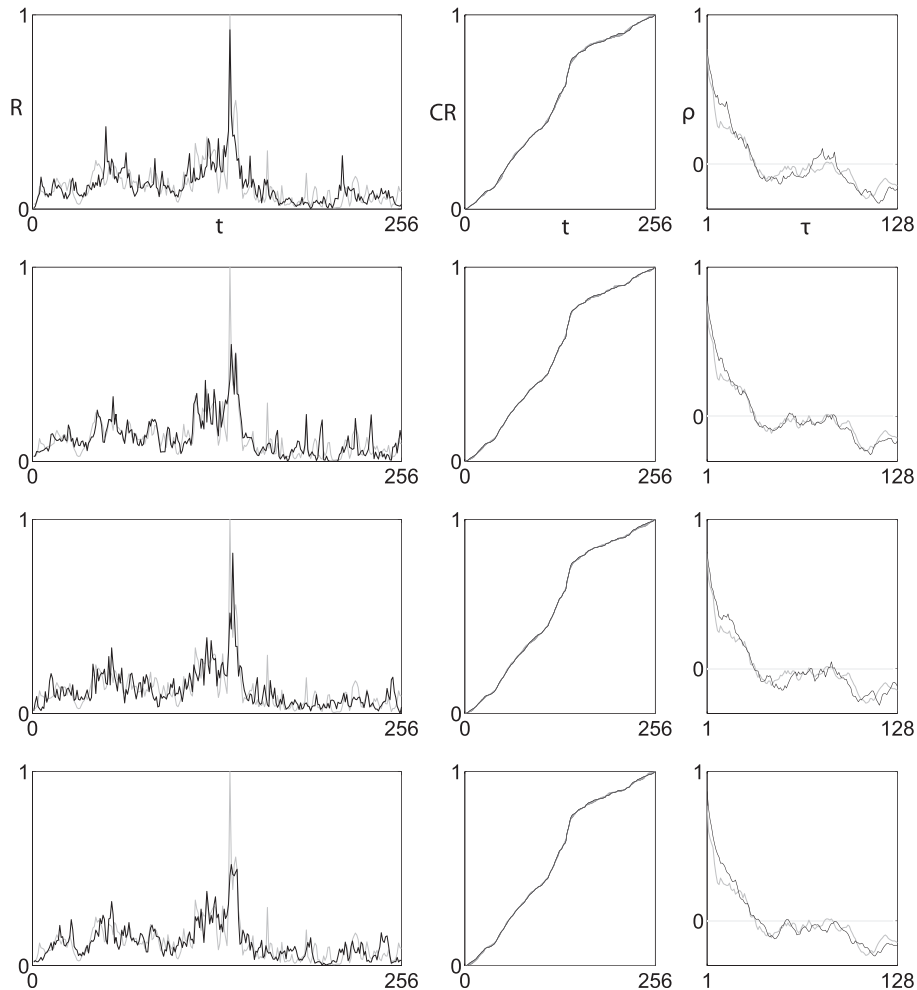
Fig. 8. Best renderings of the Boston storm from each of the four previous figures. The left two columns are the same as before, but the column on the right now depicts the autocorrelation functions with zero correlation line labeled.

approaches, all models for this storm result in renderings that, for all practical purposes, represent the observed storm.

3.1. Wire model

Fig. 4 contains the four best results obtained via the original FM approach (see Section 2.1), using representations that utilize three and four maps. The left column depicts the fit, in black, overlaying the original data, in gray. For presentation purposes, the data values have been scaled such that the highest peak in the data is given a value of 1. This plot of rainfall as a function of time (R vs. t) is followed by the cumulative of the original data, together with deviations in the fits as marked by small "lumps" along the profile (CR vs. t). Lastly, the right-most column shows the scatter plot of the data (horizontal) versus the fit (vertical), including the 10%-over and 10%-under bands. Readers interested in reconstructing the plots may navigate to the website http://puente.lawr.ucda-vis.edu/omake/jhydro2012.html, where all parameters pertaining to this and subsequent figures may be found.

Consistent with the first block in Table 4, FM-Wire, the top two rows of plots correspond to a wire using three maps, and the bottom two rows correspond to a wire defined by using four maps. While none of the fits are totally perfect, notice how the bottom two exhibit less "lumps" (in cumulative function) than the top two, and how the last one gives an extremely close approximation of the primary peak's location and magnitude, as seen on the data

set itself as well as on the top-right point on the scatter plot, which do not show bias (in all cases) in terms of over- and underestimating the original storm. All in all, the fits obtained via FM wires are excellent and represent suitable complex patterns that are nigh-indistinguishable from one another and the Boston storm.

3.2. Overlapping mapping model

Fig. 5 shows the best results obtained using the extension where the simple maps are allowed to overlap, as described in Section 2.2. As just described regarding Fig. 4 and as seen in the block FM-Leaf on Table 4, the top two rows also correspond to attractors obtained using three maps, and the bottom two correspond to leaves defined using four maps. As may be seen, these renderings produce yet other close approximations of the Boston storm that preserve various geometric features. For instance, while the top two events are fairly flat in the post-peak region of the storm, the bottom two result in more activity and hence produce better fits overall, especially with respect to Error 1 (see Table 4).

Notice how the bottom three representations gave rise to a double peak—present in the original data—at the correct timing, unlike what was seen in Fig. 4, which only contained a single fitted peak (though properly timed). Observe that, as previously found for the original FM approach, the scatter plots do not exhibit any hints of bias towards over- or underestimating, as there are roughly equal number of points above and below the shown 10% thresholds.
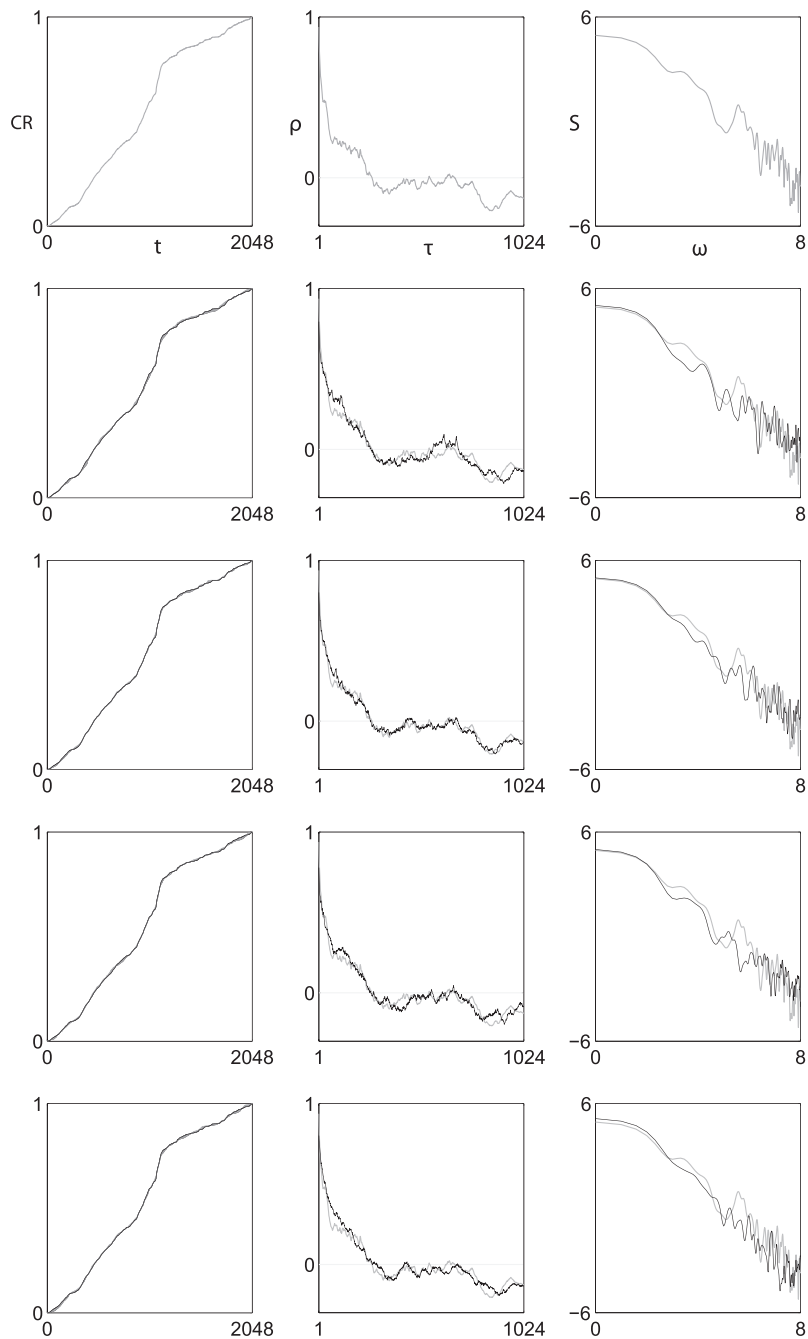
Fig. 9. Best renderings, rescaled to original resolution of 2048 points. Cumulative functions, autocorrelation functions, and power spectra (plotted in log–log) for the four best renderings in black, imposed upon that of the original Boston storm in gray From top to bottom: the original data, the original FM method, the overlapping extension, the nonlinear extension, and the higher-dimensional extension.

3.3. Nonlinear mapping model

Fig. 6 shows the counterpart obtained when the overlapping maps now contain a nonlinear cosine perturbation on the *y*-component, FM-Nonlinear as explained in Section 2.3, and using two, three, four, and four maps respectively as seen in the corresponding block in Table 4. Once again, these fits are impressive, even if not perfect, and they turn out to be comparable in quality (and not necessarily any better as one would perhaps expect) to those obtained without the additional cosine terms (see Table 4). These fits, however, exhibit additional subtle features, such as better fits in the post-peak region of the storm, as well as an accurate timing on the "dip" during the storm's early stages, particularly for the bottom two representations.

3.4. Higher dimensional mapping model

Finally, Fig. 7 includes the results obtained when generating a higher-dimensional wire (see Section 2.4) and taking the histogram of one of its marginal distributions (here, over *y*). Consistent with the FM-Marginal block on Table 4, the top two and bottom two cases of Fig. 7 were made with two and three maps, respectively. As it is the case for the three FM models considered above, no noticeable bias can be discerned from the scatter plots, and increasing the number of maps does not necessarily translate into better statistical fits. Notwithstanding the introduction of additional parameters, this model provides consistent renderings for the Boston storm. Also note how the solution represented by the last row of Fig. 7, recovers a clean double peak that closely matches

Table 5
Comparisons of the best results (starred in Table 4) at the original resolution for the Boston storm. Errors 1 and 2 are the same as in Table 4. The other attributes are defined in the text.

Procedure	# Maps	# Parameters	Error 1 (%)	Error 2 (%)	Lag (1/e)	Lag (0)	Fractal dimension	Entropy dimension	Power spectrum slope
[original data]	–	–	–	–	48	268	1.44	0.958	−1.34
FM-Wire	4	13	0.68	1.83	50	263	1.48	0.958	−1.06
FM-Leaf	4	17	0.43	1.69	54	259	1.70	0.952	−1.13
FM-Nonlinear	3	19	0.53	1.38	47	261	1.57	0.950	−1.06
FM-Marginal	3	27	0.56	1.46	60	270	1.69	0.957	−1.33

the main peaks of the storm, despite the fact that there are several low values that fall outside the 10% bands on the scatter plot, an unwelcomed feature relative to other "solutions" of the inverse problem.

3.5. A comparison of the best and scaling back to the original resolution

In order to gain a better global view of the different FM approaches, Fig. 8 compares the best "visual" results obtained via the alternative FM representations, which are also marked with asterisks in Table 4. As may be seen, such also correspond to cases that are the best overall in terms of one or more of the fitting errors, i.e., Error 1 to Error 3.

As may be discerned, the last column of Fig. 8 no longer includes the scatter plots for the fits but rather displays the autocorrelation functions (ρ vs. τ) of the data (gray) and the fits (black). As may be observed for all these renderings, the autocorrelation function and the lag associated with the first crossing of zero correlation are very close to that of the original, even though such information was not programmed into in the objective function.

As surmised from Table 4, the fits on Fig. 8 come from representations requiring four, four, three, and three maps, respectively. Given the associated parameter counts of 13, 19, 19, and 27, these faithful encodings demonstrate compression levels of 9.5:1 to 19.7:1, which grow as the resolution of the data set increases.

To illustrate what happens when the resolution of the data is increased, Fig. 9 depicts the cumulative records, autocorrelation, and power spectrum (S vs. ω) (in log–log scale) of the best results as in Fig. 8 scaled back to 2048 data points (that is, every 15 s in the original Boston storm and constructing a histogram with 2048 bins instead of 256 while inputting the same parameters into the respective FM procedures). Here it becomes particularly noticeable the closeness of the cumulative plots that do not exhibit any more lumps than they did before, indicating that performing the parameter search at a lower resolution (in this case a factor of 8) does not negatively impact the final result when rescaling back. That this is the case may be seen in the columns of Table 5 corresponding to Errors 1 and 2, for which values remain just as small at the 15-s resolution.

As may be appreciated from Fig. 8, and as one may hint given the closeness of the cumulative renderings, the autocorrelation functions and the power spectra of the FM fits lie on top of the "real" ones. This fact is also reflected in the remaining columns of Table 5, which include the lags corresponding to correlations 1/e and 0, the fractal dimension of the data and fits, the entropy dimension D_1 (a measure of the roughness and multifractality of a set, cf. Puente and Obregón, 1999), and the slope β of the power spectrum in log–log scale, as plotted. All these attributes closely mirror that of the original data, indicating indeed that the overall textures of the records are being preserved by any of those representations.

4. Summary and conclusions

We have illustrated how the FM approaches summarized herein, coupled with an effective optimization procedure for the inverse problem, can be used as an efficient tool for hydrological (geophysical) data encoding. As anticipated (e.g., Puente, 1996; Puente and Sivakumar, 2007), this geometric procedure provides a viable alternative to existing stochastic procedures that hints at the possibility of hidden determinism in natural complexity. It is proposed that the FM encoding procedures described in this work may be used to understand rainfall dynamics in a reduced geometric space, thus opening the way to novel geometric (and perhaps physical) descriptions of precipitation (Cortis et al., submitted for publication).

As the FM patterns only require a few parameters—ranging from 9 for a wire with three maps to 27 for the marginal extension with three maps—our 256-value representations result in compression ratios as high as 28:1. However, since equally faithful solutions exist for the same data sets of higher resolution (as discussed in Section 3.5), compression ratios can easily exceed 100:1 (more precisely, 157.5:1 for a projection with 2048 bins made of a wire defined with four maps). We want to emphasize here that, while the number of the FM parameters is generally larger than the typical number of parameters used in stochastic models, this does not represent a model over parameterization, as the stochastic models do not have enough "knobs" to adequately capture the finest details of typical precipitation datasets.

These highly promising results, and others for different sites that will be reported elsewhere, represent a definite step forward with respect to previous attempts (e.g., Puente and Obregón, 1996; Obregón et al., 2002a, 2002b) and substantiate the idea that complex rainfall patterns may be wholly characterized in a deterministic fashion.

Given the recent reports of precipitation measurements being plagued with nontrivial errors (Lanza and Vuerich, 2009), it may also be argued that all representations herein, with maximum deviation from cumulative deviations (at the original resolution) of no more than 2%, are acceptable renderings of what may happen in nature, for all major peaks and trends in all sets considered are sufficiently preserved.

References

Barnsley, M.F., 1988. Fractals Everywhere. Academic Press, San Diego, CA.

Cortis, A., Puente, C.E., Sivakumar, B., 2009. Nonlinear extensions of a fractal–multifractal approach for environmental modeling. Stoch. Environ. Res. Risk A 23, 890–906.

Cortis, A., Puente, C.E., Huang, H.-H., Maskey, M.L., Sivakumar, B., Obregón, N., 2013. A physical interpretation of the deterministic fractal–multifractal method as a realization of a generalized multiplicative cascade. Stoch. Environ. Res. Risk A (submitted for publication).

Fernández Martínez, J.L., García Gonzalo, E., Fernández Álvarez, J.P., Kuzma, H.A., Menéndez Pérez, C.O., 2010. PSO: a powerful algorithm to solve geophysical inverse problems. Application to a 1D-DC resistivity case. J. Appl. Geophys. 71 (1), 13–25.

Hitchcock, F.L., 1941. The distribution of a product from several sources to numerous localities. J. Math. Phys. 20, 224–230.

Kennedy, J., Eberhart, R.C., 1995. Particle swarm optimization. In: Proceedings of the IEEE International Joint Conference on Neural Networks. IEEE Service Center, Piscataway, NJ, pp. 1942–1948.

Lanza, L.G., Vuerich, E., 2009. The WMO field intercomparison of rain intensity gauges. Atmos. Res. 94 (4), 534–543.

Lovejoy, S., Schertzer, D., 1990. Multifractals, universality classes and satellite and radar measurements of cloud and rain fields. J. Geophys. Res. 95 (3), 2021–2034.

Obregón, N., Puente, C.E., Sivakumar, B., 2002a. Modeling high resolution rain rates via a deterministic fractal–multifractal approach. Fractals 10 (3), 387–394.

Obregón, N., Sivakumar, B., Puente, C.E., 2002b. A deterministic geometric representation of temporal rainfall. Sensitivity analysis for a storm in Boston. J. Hydrol. 269 (3–4), 224–235.

Puente, C.E., 1996. A new approach to hydrologic modeling: derived distributions revisited. J. Hydrol. 187, 65–80.

Puente, C.E., 2004. A universe of projections: may Plato be right? Chaos Solitons Fract. 19 (2), 241–253.

Puente, C.E., Obregón, N., 1996. A deterministic geometric representation of temporal rainfall: results for a storm in Boston. Water Resour. Res. 32 (9), 2825–2839.

Puente, C.E., Obregón, N., 1999. A geometric Platonic approach to multifracticality and turbulence. Fractals 7 (4), 403–420.

Puente, C.E., Sivakumar, B., 2007. Modeling hydrologic complexity: a case for geometric determinism. Hydrol. Earth Syst. Sci. Discuss. 11, 721–724.

Rodríguez-Iturbe, I., 1986. Scale of fluctuation of rainfall models. Water Resour. Res. 22 (9), 15S–37S.

Rodríguez-Iturbe, I., Febres de Power, B., Sharifi, M., Georgakakos, K.P., 1989. Chaos in rainfall. Water Resour. Res. 25 (7), 1667–1675.

Tessier, Y., Lovejoy, S., Schertzer, D., 1993. Universal multifractal: theory and observations for rain and clouds. J. Appl. Meteorol. 32, 223–250.